Impact of multiple RIS on channel characteristics: An experimental validation in Ka band

Taghrid Mazloum, Luca Santamaria, Frederic Munoz, Antonio Clemente, Jean-Baptiste Gros, Youssef Nasser, Mikhail Odit, Geoffroy Lerosey, Raffaele d'Errico

Impact of Multiple RIS on Channel Characteristics: An Experimental Validation in Ka Band

Taghrid Mazloum*‡, Luca Santamaria†, Frederic Munoz*‡, Antonio Clemente*‡, Jean-Baptiste Gros†, Youssef Nasser†, Mikhail Odit†, Geoffroy Lerosey†, and Raffaele D'Errico*‡
*CEA-Leti, 17 rue des Martyrs 38054 Grenoble, France
Email: see {taghrid.mazloum, frederic.munoz, raffaele.derrico}@cea.fr
‡Université Grenoble-Alpes, Grenoble, France
†Greenerwave, 35 rue du Sentier, 75002 Paris, France

***Abstract*—In this work, we present the results of an experimental validation of the use of multiple Reconfigurable Intelligent Surfaces (RISs) in indoor scenarios. The setup employs a Transmitting and a Reflecting RIS in the Ka band with more than 400 elements each. Two different 1-bit Unit Cell (UC) based on PIN-diode technologies have been designed to realize the RISs. The Transmitting RIS (T-RIS) is used on the Base Station (BS) side to perform steering towards the User Equipment (UE), or the Reflecting RIS (R-RIS) acting as extender. The channel responses are analysed over a wide band (25-35 GHz) to investigate the impact of the phase distribution over RISs, as well as the antenna employed on the BS or UE side. Finally, the Multi Path Components (MPCs) in different Line of Sight and Obstructed Line of Sight, are estimated by means of space-alternating generalized expectation-maximization (SAGE) wideband algorithm, and analysed to highlight the use of RISs.**

***Index Terms*—RIS, programmable electromagnetic surface, transmitarray, reflectarray, mmWave propagation, measurements.**

I. Introduction

In order to achieve the performance requirements of the next 6th Generation (6G) networks, there has been an increasing interest in Reconfigurable Intelligent Surfaces (RISs) [1] as a hardware-efficient way to realize desired dynamic manipulation on the signal propagation environment in wireless communications [2], [3]. The modeling of signal propagation in such RIS-empowered scenarios appears very challenging [4].

Recently, several RISs have been designed and fabricated for different purposes related to 6G research. Most of the RIS-enabled channel measurements and experiments in the literature are conducted in anechoic chamber or relatively simple indoor environments, generally employing horn antennas or reflectarray modes [5], [6]. A channel reciprocity investigation was conducted by placing two horn antennas in front of the RIS to minimize the effects of multipath components (MPCs) other than the one reflected by the RIS [7]. RIS with continuous phase was employed for backscattering communications with monopole antennas at very short distance (less than 1 m) [8]. In [9] the RIS extender, also employed in this work, was used together with horn antennas to prove the boosted connectivity in an indoor obstructed scenario, by creating a line of sight (LOS) propagation for signal improvement and transmit QPSK modulated signals.

Besides the use of RIS in reflecting mode (R-RIS), these surfaces can be designed to work in transmitting mode (T-RIS) and employed to realize transmitarrays [10]. These technologies can efficiently enable beamforming which is especially required for millimeter wave communication suffering from high propagation losses [11]. In [12], the impact of T-RIS on the channel characteristics was investigated using at one side a monopole antenna.

Going beyond the previous works in literature, we intend here to present a channel measurement campaign employing simultaneously two different types of RIS: a T-RIS on the Base Station (BS) side and a R-RIS acting as extender. Instead of using directive antennas pointing towards the RIS, we employed a monopole, whose characteristics are emulating User Equipment (UE) antenna. To estimate the impact of RIS, the MPCs are shown in time-angular domains, by employing a virtual array on UE side combined with high resolution algorithm (SAGE). This approach is compared to the ones commonly used in literature, to prove the modification of MPCs, thanks to the use of two RIS. In section II, we present the two RIS designs based on PIN diode technology. Section III presents the channel measurement setup and campaign. Section IV presents the preliminary results on the Channel Frequency Response (CFR) and Power Delay Profile (PDP), as well as in the angular domain.

II. RIS designs and protoypes

A. 1-bit Transmitting RIS

The employed linearly-polarized T-RIS operates in the Ka-band over a 3-dB relative gain bandwidth close to 25%. A 10-dBi pyramidal horn antenna illuminates a programmable electromagnetic surface composed of 20×20 radiating elements (also named unit cells). These unit cells (UC) are based on a 1-bit architecture to achieve low power consumption. To this purpose, two phase-states with a relative phase-shift of 180° are achieved by electronically changing the state of two PIN diodes integrated on the UC. The UC architecture is presented in Fig. 1(a) and consists of four metal layers (M1 – M4), two identical substrates of Rogers Duroid RT6002 and one bonding film of Arlon CuClad 6700. Fig. 1(b) shows the view of the T-RIS with the focal source and the steering logic. The transmitting layer (M4) is composed of a rectangular patch loaded by a U-shaped slot, while the receiving layer (M1)

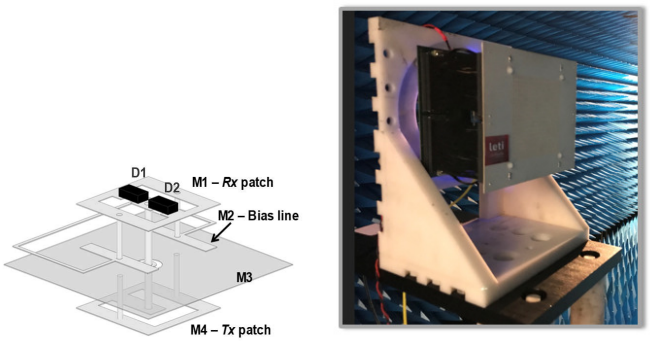

(a) (b)

Fig. 1. Schematic view of the 1-bit electronically reconfigurable unit cell based on PIN diodes (a), view of the T-RIS with the focal source and the steering logic (b).

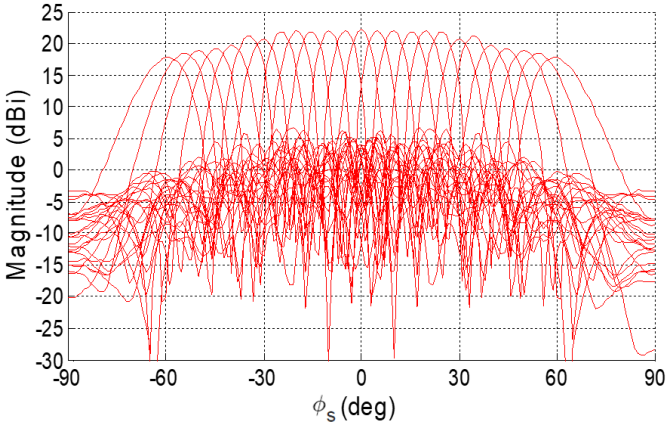

Fig. 2. Linearly-polarized T-RIS beam scanning capability at 28 GHz (simulations).

contains a rectangular patch loaded by an O-shaped slot and the two PIN diodes (D1 and D2). In the EM simulator, these active devices are modelled as a lumped-element equivalent circuit extracted from the measurements and a gallium-arsenide block [13]. This active patch is connected to the passive one printed on (M4) with a metallized via hole placed at the center of the UC. A ground plane occupies one of the two intermediate metal layers (M3). The other inner layer (M2) contains the biasing lines. In the proposed UC structure, one PIN diode is biased in the forward state with a 5-mA current. The 1.3-V threshold voltage of this diode is sufficient to maintain the other diode, mounted in anti-parallel configuration, in its reverse state. Thus, only one bias line is necessary for each UC, facilitating thereby the layout and routing of the bias network in very large array configurations. The bias line is 100-μm wide and is connected to the active patch by using two symmetric metallic via connections. More details on the 1-bit unit-cell operational principle, model, parametric analysis, and simulation setup are detailed in [13]. The array can electronically steer the beam on a two dimensional window of $120° \times 120°$. The T-RIS patterns are shown in Fig. 2. A peak gain of 23.1 dBi has been measured at 28 GHz when the beam is oriented in the broadside direction in very good agreement with the simulations. The average gain reduction due to the pin-diode insertion loss if compared to the performance of an equivalent fixed-beam transmitarray is lower than 1.7 dB.

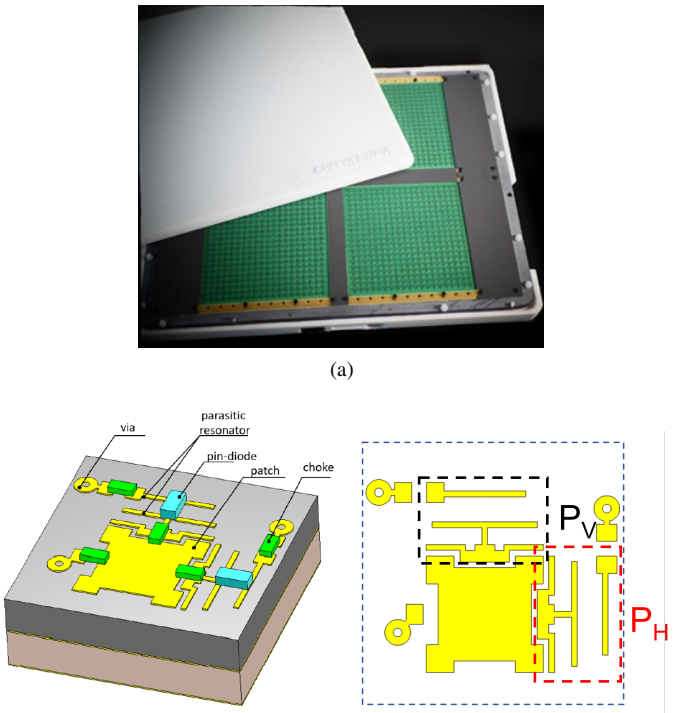

(a) (b) (c)

Fig. 3. R-RIS composed by 4 panels of 20×20 pixels (a). Perspective view (b), and layout (c) of the R-RIS unit cell.

B. 1-bit Reflecting RIS

In this section, we describe Reflecting-RIS (R-RIS) design working at mmW frequencies. The proposed R-RIS is shown in Fig. 3(a). The unit cell has been designed to provide the patch resonance f_0 to be approximately around 27.5 GHz. The simplest way to achieve a 180^o phase shift is to shunt the patch resonator onto the ground using an active element i.e. PIN diode. Nevertheless, this leads first to a strong dissipation growth due to increased current through the PIN diode. Here the design of the pixel, shown in Fig. 3 (b) and (c), is complemented with a parasitic resonator P_H and P_V for both corresponding horizontal and vertical polarization of the E-vector of the incident wave. The resonance frequency of the parasitic resonator lies close to the resonance of the patch. That leads to the appearance of strong coupling between two resonators and corresponding anti-crossing behavior when coupled resonances repulse and the mutual resonance shifting occurs. While changing the electrical length of the parasitic resonator we change its resonance frequency and can tune the mutual coupling between resonant modes of the parasitic resonator and the patch. This allows to change the resonance frequency of the patch and the phase of the reflected wave at a given frequency. A 10×10 cm² RIS made up of 400 unit cells periodically

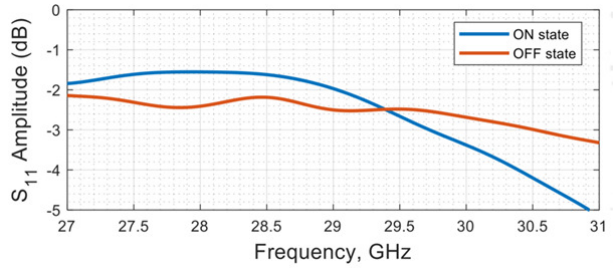

(a)

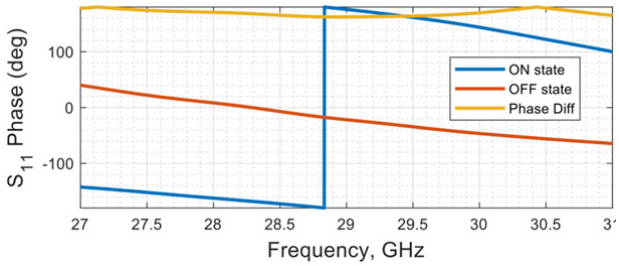

(b)

Fig. 4. R-RIS Unit Cell characteristics: reflection coefficient amplitude (a), phase (b).

placed every $\lambda/2 = 0.5$ cm on a rectangular lattice of 20×20 pixels. Each unit cell having to control independently both components of the reflected EM field. An overall of 400 diodes are used to control the vertical polarization and 400 diodes to control horizontal polarization. RIS consists of six layers PCB. The first layer is made from a low-loss substrate, namely the METEORWAVE 8000 from AGC of 0.5 mm thickness and $\epsilon_r = 3$ dielectric permittivity, and supports the 400 unit cells. The five remaining layers are made from FR4 substrate. The last layer supports the electronic components to control the states of the diodes of the pixels on the first layer. This control is operated by a 10×10 matrix of shift registers, each managing the states of 8 PIN diodes associated to the horizontal and vertical polarization states of 4 pixels. In order to provide control of each pixel of the RIS, an FPGA control board has been designed and programmed. PIN diodes are thus connected to the control board through the network of shift registers. We have chosen to use a bistatic characterization approach. Fig. 4 shows the amplitude and the phase of the measured $|S_{11}|$. As can be seen, the reflecting surface maintains an average dissipation of -2 dB in the 27-31 GHz band. In the desired mmW frequency range, the phase difference between ON and OFF states is between $150°$ and $180°$. The physical model of the binary R-RIS design, its fabrication and characterization are detailed in [14], [9], [15], [16].

III. Channel Measurement Campaign

The RIS assisted wireless communication channel has been measured and characterized in an indoor environment. The floorplan and the measurement environment are shown in Fig. 5. Three different setups were considered:

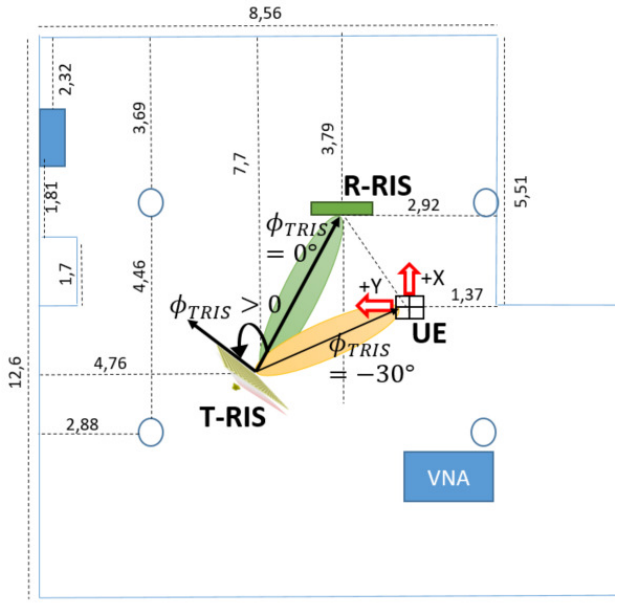

(a)

(b)

Fig. 5. Multiple RIS channel measurement campaign: floorplan (a) and environment (b).

- Setup 1: Reflective RIS (extender mode) with two far-away horn antennas (horn-horn)
- Setup 2: Reflective RIS (extender mode) with one horn antenna and one monopole antenna (horn-monopole)
- Setup 3: Reflective RIS (extender mode) with one T-RIS and one monopole antenna (TRIS-monopole)

The R-RIS, the T-RIS, the horn antenna and the monopole antenna are almost at the same height, about 1.6 m above the ground. The propagation channel is measured based on a vector network analyser (VNA) operating in the 25-35 GHz frequency range. On the UE side in Setup 2 and Setup 3, the monopole antenna is placed on a X-Y positioner and thus performs a 3×3 spatial grid of a half-wavelength step (4.3 mm). A computer is employed in order to control the measurement equipment (i.e., the VNA and the positioner) as well as configure the phase distributions of the T-RIS and the R-RIS. Indeed, the R-RIS involves an optimization algorithm in order to steer the

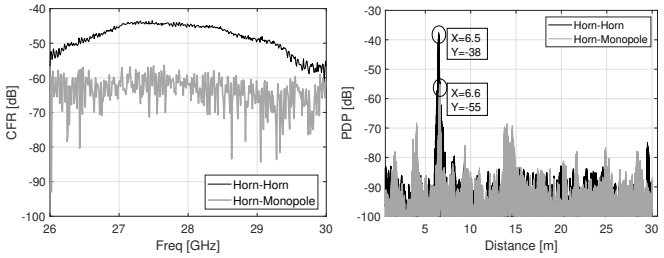

(a) (b)

Fig. 6. Comparison of Setup 1 (horn-horn) and Setup 2 (horn-monopole): CFR (a) and PDP (b).

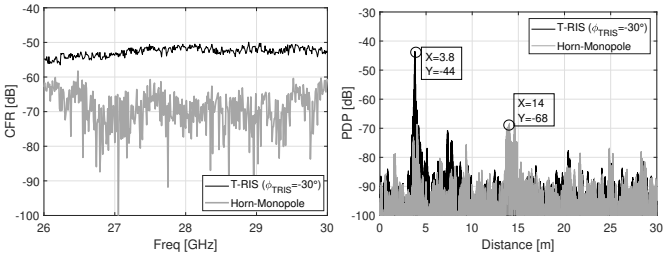

(a) (b)

Fig. 8. Comparison of Setup 2 and Setup 3, use of T-RIS steering towards UE (R-RIS OFF): CFR (a) and PDP (b).

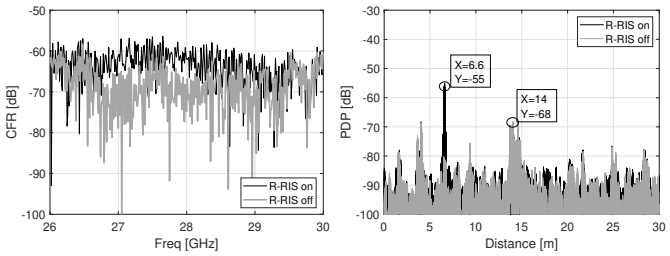

(a) (b)

Fig. 7. Setup 2 (horn-monopole), effect of R-RIS: CFR (a) and PDP (b).

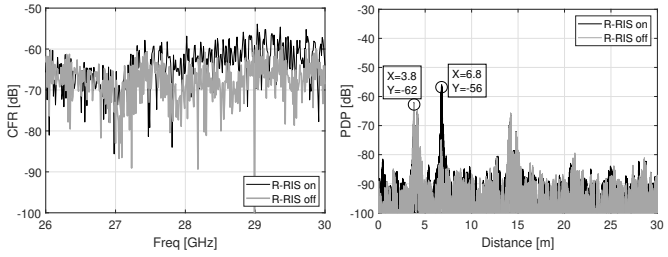

(a) (b)

Fig. 9. Setup 3, use of T-RIS steering towards R-RIS (ON and OFF): CFR (a) and PDP (b).

beam towards the receiver (RX), for a given location of the transmitter (TX). The optimization algorithm will set the phase distributions of the R-RIS based on an estimate of the TX and RX coordinates, that maximizes the CFR at the RX side (by means of a feedback based on the S21 parameter measured by the VNA). For each TX-RX locations, the optimization algorithm is launched to find the optimal beam at the operating frequency of the R-RIS, i.e., 28 GHz with a narrow bandwidth of 1 GHz.

IV. Results

A. RIS and Antenna effect on Channel Functions

In this section, we present the preliminary results of the measurement campaign, by considering both the CFR and the PDP. Here, the PDP is plotted as a function of distance. Fig. 6 shows a comparison between the Setup 1 (horn-horn) when two horn antennas are pointed directly to the R-RIS, and Setup 2 (horn-monopole) when one of the horns is replaced by the monopole. Setup 2 results are also shown in Fig. 7 for a comparison between R-RIS ON and OFF. While the use of R-RIS is clearly visible in the CFR when using horn antennas, when a monopole is employed the gain in the frequency domain can be hardly estimated (see Fig. 6 (a) and Fig. 7 (a)). However the PDP in Fig. 6 (b) clearly shows the MPCs richness when employing a monopole antenna and a common principal MPC corresponding to the R-RIS related path and coming at 6.5 m. We can appreciate that this path presents a difference of around 17 dB, which actually corresponds to the realized gain difference between using a horn or a monopole antenna in the RIS direction. While employing a monopole antenna (Setup 2), even though turning either ON or OFF the R-RIS will not strongly affect the CFR (Fig. 7 (a)), the PDP will remain almost the same with the modification of the only MPC corresponding to the R-RIS related path (at 6.5 m). This modification of the R-RIS related path is clearly shown in Fig. 7 (b).

Overall channel gain can be improved by beamforming towards the UE. In Setup 3, we use the T-RIS to this purpose. Fig. 8 shows how the LOS path, here at around 3.8 m, is enhanced thanks to the phase distribution optimization towards a direction of departure at $\phi_{TRIS} = -30°$, corresponding to the direction of UE. Also, the impact of such an improvement is clearly shown in the CFR results, compared with a horn antenna at the TX side (Setup 2).

The T-RIS can be hence used to point towards the UE, as shown above, or eventually towards the R-RIS (with a steering angle of $\phi_{TRIS} = 0°$), whose phase distribution is optimized in the direction of UE. Fig. 9 shows the channel acquisition employing both RIS. The T-RIS is pointing towards the R-RIS, which is turned either ON or OFF. In particular we highlight in the PDP that only the R-RIS path is affected, while other MPCs are mostly unchanged.

B. RIS effect on MPCs Spatial Characteristics

We performed an azimuthal angular scanning of the environment using the T-RIS, by measuring the channel for each steering angle ϕ_{TRIS} varying between $-60°$ and $+60°$, with a step of $5°$. For each steering angle, we employed a virtual (3×3) array approach at UE side and high-resolution UWB SAGE algorithm [17]. This allows better visualization of the MPCs manipulation and identifying the MPCs in distance and angle

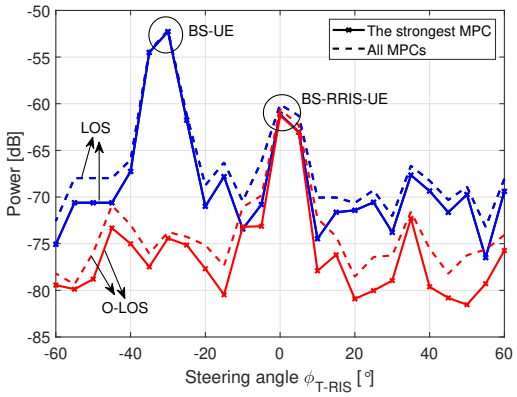

Fig. 10. MPCs power as function fo T-RIS steering in setup 3: LOS (blue), O-LOS (red).

of arrival (AoA). After applying the UWB SAGE algorithm, the amplitude of the strongest MPCs and the sum of the power of the resolved MPCs are obtained for each value of ϕ_{TRIS}.

The results are shown in Fig. 10 for both LOS and O-LOS (Obstructed-LOS) cases, where in the latter an object obstructs the path between the T-RIS and the UE. The obstacle consists into a metallic plate of size 0.58m×0.58m, placed at 1.65 m height. This would realize a partial obstruction of the LOS path, but diffraction on the plate borders, as well as bounces on the ceiling and the floor could be present in this case. Regarding the LOS case, it is clear that the channel gain is significant for merely two cases, i.e., when the T-RIS is steering towards the UE at $\phi_{TRIS} = -30°$ and towards the R-RIS at $\phi_{TRIS} = 0°$. Each one of these paths dominates the corresponding MPC channel. At $\phi_{TRIS} = 0°$ the slight difference between the powers of the strongest MPC and all MPCs is due to the direct T-RIS path provided by the sidelobes. For the O-LOS case, the only way to perform a high channel gain is through the R-RIS.

Fig. 11 and Fig. 12 show the spatial characteristics of the extracted MPCs, in LOS and O-LOS scenarios. Each MPC is graphically represented by a point on the angle-distance axes, and its color is related to its amplitude (in dB).

In the case where the R-RIS is OFF and the BS is steering towards the UE ($\phi_{TRIS} = -30°$) in LOS, a main path of -52 dB amplitude appears at 3.75 m and with an AoA of 135°, which corresponds to the direct BS to UE path. Another MPC appears at 4.2 m and with 134° as an AoA, but with a very low power -72 dB. This MPC is due to reflections from the ceiling and is common with the O-LOS case, where the direct BS to UE path disappears. This result is also shown in Fig. 10 with a R-RIS ON because the direct BS to UE path is not impacted by the state of the R-RIS. In the case where the BS is steering towards the R-RIS, i.e. $\phi_{TRIS} = 0°$, the direct BS to UE path is still present, but with a very low amplitude (less than -70 dB), due to T-RIS gain reduction. This loss is in line with the sidelobe level shown in Fig. 2. When using the R-RIS and optimising its phase distribution, a significant MPC at 6.75 m and with an AoA of 43° is generated, as shown in Fig. 11 (c) and Fig. 12 (c). This R-RIS path has a power of

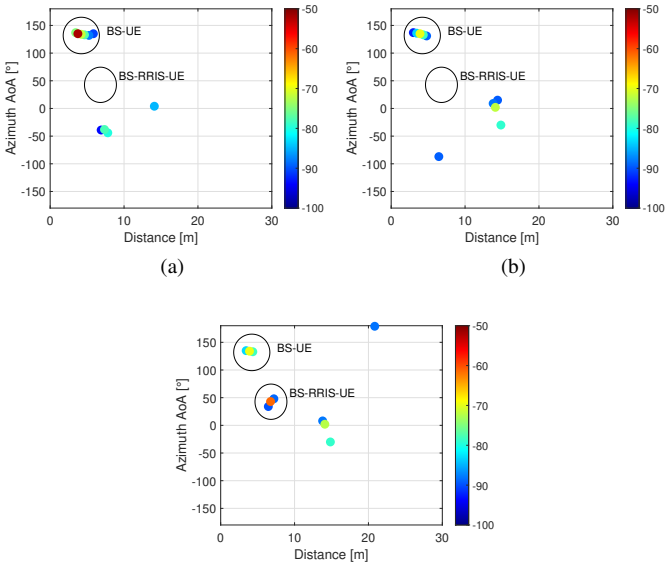

Fig. 11. MPCs distribution in LOS: R-RIS OFF $\phi_{TRIS} = -30°$ (a), R-RIS OFF $\phi_{TRIS} = 0°$ (b), R-RIS ON $\phi_{TRIS} = 0°$ (c).

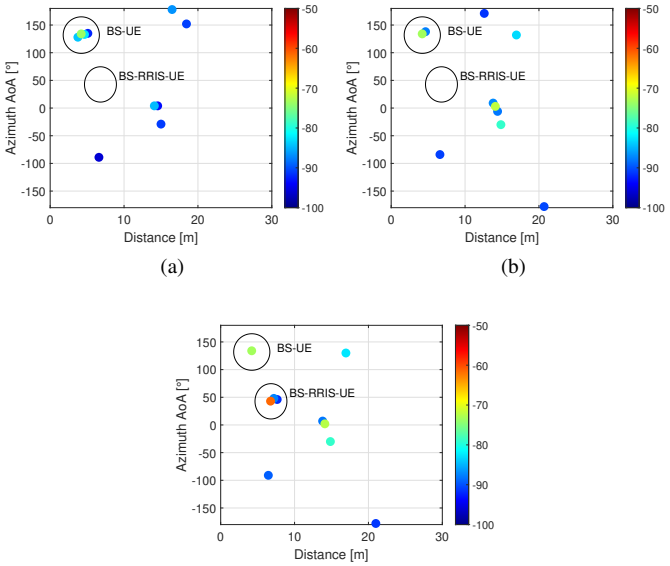

Fig. 12. MPCs distribution in O-LOS: R-RIS OFF $\phi_{TRIS} = -30°$ (a), R-RIS OFF $\phi_{TRIS} = 0°$ (b), R-RIS ON $\phi_{TRIS} = 0°$ (c).

-61 dB, which is at least 10 dB higher than the direct path BS-UE.

V. Conclusions and Perspectives

In the present work, we present a channel measurement campaign at mmWave employing two different RISs in transmitting and reflecting modes, both based on PIN diode technology at unit cell to realize 1-bit phase quantization. With respect to the previously presented results, this work uses a more

realistic condition where the UE antenna is not a directional one precisely pointing towards the RIS, but a wideband monopole with omnidirectional pattern in the azimuth plane. While using this antenna makes the appreciation of the RIS contribution more sensitive to analyze in the frequency domain, the overall channel gain can be improved by using T-RIS to perform beamforming towards the UE. While T-RIS scans the azimuth plane, a significant R-RIS path is remarkable when T-RIS steers towards the R-RIS, whose phase distribution is optimized. This modified MPC is clearly identified in the delay domain and also in the delay-angular domain, after applying a high-resolution algorithm (SAGE). The obtained results allow proving the concept basis of RIS-enabled coverage and localization enhancement purposes. Further works will include additional measurements, including multi-user scenario and blocking effects.

ACKNOWLEDGMENT

This work was supported in part by the EU H2020 RISE-6G project under grant 101017011. The authors are thankful to Gloria Makhoul for the fruitful discussions during the measurement campaign preparation.

REFERENCES

[1] E. C. Strinati, G. C. Alexandropoulos, H. Wymeersch, B. Denis, V. Sciancalepore, R. D'Errico, A. Clemente, D.-T. Phan-Huy, E. De Carvalho, and P. Popovski, "Reconfigurable, intelligent, and sustainable wireless environments for 6g smart connectivity," *IEEE Communications Magazine*, vol. 59, no. 10, pp. 99–105, 2021.

[2] N. Kaina, M. Dupre, G. Lerosey, and M. Fink, "Erratum: Shaping complex microwave fields in reverberating media with binary tunable metasurfaces," *Scientific Reports*, vol. 4, p. 6693, 10 2014.

[3] N. Kaina, M. Dupré, M. Fink, and G. Lerosey, "Hybridized resonances to design tunable binary phase metasurface unit cells," *Opt. Express*, vol. 22, pp. 18881–18888, Aug 2014.

[4] M. Di Renzo, A. Zappone, M. Debbah, M.-S. Alouini, C. Yuen, J. De Rosny, and S. Tretyakov, "Smart radio environments empowered by reconfigurable intelligent surfaces: How it works, state of research, and the road ahead," *IEEE journal on selected areas in communications*, vol. 38, no. 11, pp. 2450–2525, 2020.

[5] L. Dai, B. Wang, M. Wang, X. Yang, J. Tan, S. Bi, S. Xu, F. Yang, Z. Chen, M. D. Renzo, C.-B. Chae, and L. Hanzo, "Reconfigurable intelligent surface-based wireless communications: Antenna design, prototyping, and experimental results," *IEEE Access*, vol. 8, pp. 45913–45923, 2020.

[6] W. Tang, M. Z. Chen, X. Chen, J. Y. Dai, Y. Han, M. Di Renzo, Y. Zeng, S. Jin, Q. Cheng, and T. J. Cui, "Wireless communications with reconfigurable intelligent surface: Path loss modeling and experimental measurement," *IEEE Transactions on Wireless Communications*, vol. 20, no. 1, pp. 421–439, 2021.

[7] Z. Wang, L. Tan, H. Yin, K. Wang, X. Pei, and D. Gesbert, "A received power model for reconfigurable intelligent surface and measurement-based validations," in *2021 IEEE 22nd International Workshop on Signal Processing Advances in Wireless Communications (SPAWC)*, pp. 561–565, IEEE, 2021.

[8] R. Fara, P. Ratajczak, D.-T. Phan-Huy, A. Ourir, M. Di Renzo, and J. De Rosny, "A prototype of reconfigurable intelligent surface with continuous control of the reflection phase," *IEEE Wireless Communications*, vol. 29, no. 1, pp. 70–77, 2022.

[9] V. Popov, M. Odit, J.-B. Gros, V. Lenets, A. Kumagai, M. Fink, K. Enomoto, and G. Lerosey, "Experimental demonstration of a mmWave passive access point extender based on a binary reconfigurable intelligent surface," *Frontiers in Communications and Networks*, vol. 2, 2021.

[10] A. Clemente, L. D. Palma, F. Diaby, L. Dussopt, K. Pham, and R. Sauleau, "Electronically-steerable transmitarray antennas for ka-band," in *2019 13th European Conference on Antennas and Propagation (EuCAP)*, pp. 1–4, 2019.

[11] S. Kutty and D. Sen, "Beamforming for millimeter wave communications: An inclusive survey," *IEEE Communications Surveys & Tutorials*, vol. 18, no. 2, pp. 949–973, 2016.

[12] A. Mudonhi, M. Lotti, A. Clemente, R. D'Errico, and C. Oestges, "Impact of a transmitting-RIS on the geometrical structure of indoor mmWave channels," in *2022 16th European Conference on Antennas and Propagation (EuCAP)*, pp. 1–5, 2022.

[13] L. Di Palma, A. Clemente, L. Dussopt, R. Sauleau, P. Potier, and P. Pouliguen, "1-Bit Reconfigurable Unit Cell for Ka-Band Transmitarrays," *IEEE Antennas and Wireless Propagation Letters*, vol. 15, pp. 560–563, 2016.

[14] J.-B. Gros, V. Popov, M. A. Odit, V. Lenets, and G. Lerosey, "A reconfigurable intelligent surface at mmWave based on a binary phase tunable metasurface," *IEEE Open Journal of the Communications Society*, vol. 2, pp. 1055–1064, 2021.

[15] G. Lerosey, "From reconfigurable intelligent surfaces to mmwave beamforming," *MICROWAVE JOURNAL*, vol. 65, no. 8, pp. 22–40, 2022.

[16] J.-B. Gros, V. Popov, M. Odit, and G. Lerosey, "A wave physics approach to electronically steerable antennas," *Small Satellite Conference*, 2021.

[17] B. Fleury, M. Tschudin, R. Heddergott, D. Dahlhaus, and K. Ingeman Pedersen, "Channel parameter estimation in mobile radio environments using the SAGE algorithm," *IEEE Journal on Selected Areas in Communications*, vol. 17, no. 3, pp. 434–450, 1999.